Beyond Standard Model Searches in the MiniBooNE Experiment

Teppei Katori[1] and Janet Conrad[2]

[1]Queen Mary University of London, London, E1 4NS, U.K.
[2]Massachusetts Institute of Technology, Cambridge, MA 02139, USA

May 1, 2014

Abstract

The MiniBooNE Experiment has contributed substantially to beyond standard model searches in the neutrino sector. The experiment was originally designed to test the $\Delta m^2 \sim 1$ eV^2 region of the sterile neutrino hypothesis by observing ν_e ($\bar{\nu}_e$) charged current quasi-elastic signals from a ν_μ ($\bar{\nu}_\mu$) beam. MiniBooNE observed excesses of ν_e and $\bar{\nu}_e$-candidate events in neutrino and anti-neutrino mode, respectively. To date, these excesses have not been explained within the neutrino Standard Model (νSM), the Standard Model extended for three massive neutrinos. Confirmation is required by future experiments such as MicroBooNE. MiniBooNE also provided an opportunity for precision studies of Lorentz violation. The results set strict limits for the first time on several parameters of the Standard Model-Extension, the generic formalism for considering Lorentz violation. Most recently, an extension to MiniBooNE running, with a beam tuned in beam-dump mode, is being performed to search for dark sector particles. This review describes these studies, demonstrating that short baseline neutrino experiments are rich environments in new physics searches.

1 Introduction

Across the particle physics community, the mysterious periodic-table-like nature of the Standard Model (SM) is motivating searches for new particles, new forces and new properties of the particles that are known. The neutrino sector is proving a rich environment for these searches. Having already found one beyond-Standard-Model (BSM) effect–neutrino mass [1]–a series of experiments are pursuing other potential signals. Unlike the case of three-neutrino oscillation measurements within νSM, many of these searches are pursued over short baselines, from a few meters to approximately a kilometer. The Mini Booster Neutrino Experiment (MiniBooNE) at Fermi National Accelerator Laboratory (Fermilab) is an excellent example, having contributed substantially to BSM studies.

This review describes the MiniBooNE BSM program. We begin by describing the experiment. This is followed by a discussion of the MiniBooNE cross section studies, which have been essential input to both the BSM searches within this experiment, and also to other experiments, including T2K most recently [2]. We then describe three searches: the sterile neutrino search which motivated the experiment, Lorentz violation searches which set the first limits on five neutrino sector parameters, and the search for dark sector particles which is now being pursued with a re-configured beam.

2 MiniBooNE experiment

MiniBooNE (running from 2002-2012) was originally designed to test the LSND signal [3]. In the LSND experiment, low energy (0 to 53 MeV) muon anti-neutrinos were produced by pion decay-at-rest (DAR), and were detected by the liquid-scintillator-based LSND detector at 31 m from the target. The observed 3.8σ excess of $\bar{\nu}_e$ candidate events could be interpreted as oscillations in the $\Delta m^2 \sim 1$ eV^2 region within a simple two massive neutrino oscillation hypothesis, where the oscillation probability is given by:

$$P(\bar{\nu}_\mu \to \bar{\nu}_e) = \sin^2 2\theta \sin^2(1.27\Delta m^2 L/E). \quad (1)$$

Here, θ and Δm^2 are oscillation parameters to control the amplitude and the period, respectively (further discussed in Section 4), L is the distance from neutrino production to interaction in meters, and E is the energy of the neutrino in MeV.

An experiment which maintains the same L/E ratio should observe an oscillation probability consistent with LSND if the simple two neutrino model is a good approximation of the underlying effect. However, by employing an average E which is an order of magnitude larger then LSND, the systematic errors associated with production and decay are quite different. If L is increased accordingly, and no signal is observed, this rules out the two neutrino oscillation hypothesis of the LSND result.

MiniBooNE was designed with this in mind. The MiniBooNE beam peaked at ∼700 MeV and the Cherenkov detector was located at ∼500 m baseline. Fig. 1 shows an overview of the MiniBooNE design [4], and in the remainder of this section we provide more details.

2.1 Booster Neutrino Beam-line

The Booster Neutrino Beam-line (BNB) extracts 8 GeV kinetic energy protons from the Fermilab Booster, a 149 m diameter synchrotron (Fig. 1, top left). Eighty one bunches, separated in time by ∼19 ns, are extracted by a fast kicker within a ∼ 1.6 μs pulse. Each pulse contains around

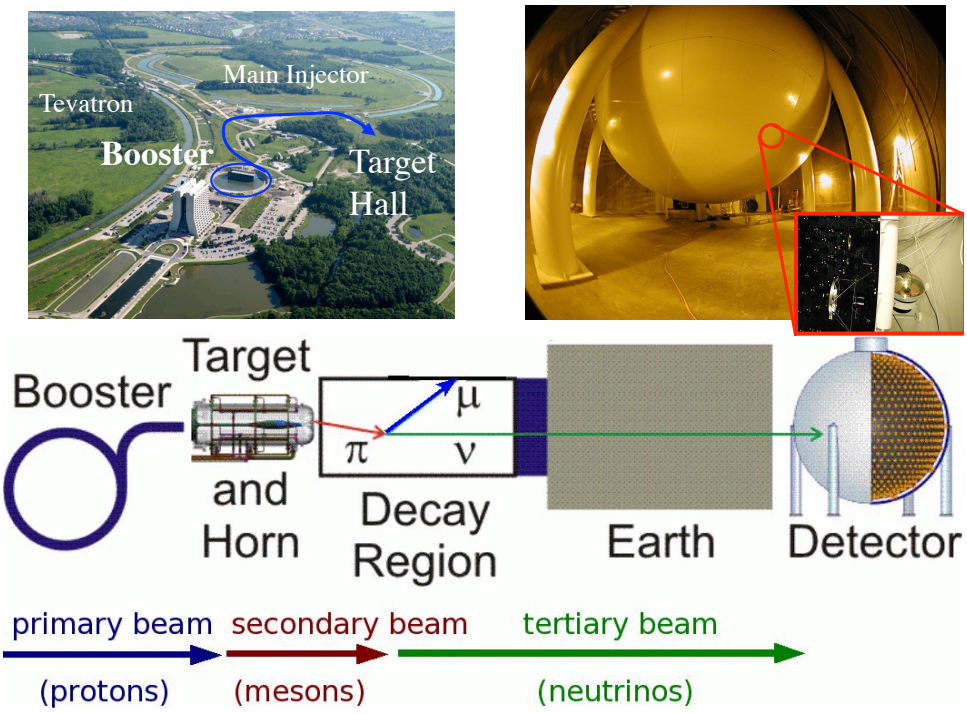

Figure 1: The MiniBooNE experiment layout [4]. Top left: the Fermilab accelerator complex. Top right: the MiniBooNE detector, with inset showing the black inner volume and the white outer volume. Bottom: Schematic layout of the beam and detector [5].

4×10^{12} protons. Typically, four to five pulses per second were sent to BNB to produce the neutrino beam.

This high intensity proton pulse collides with a beryllium target to produce a shower of mesons (Fig. 1, bottom). The target is located within a magnetic focusing horn. For neutrino mode running, the toroidal field generated by the horn focuses positive mesons, with π^+ decay-in-flight (DIF) as the primary source of the ν_μ beam. In anti-neutrino mode running, the horn focuses negative mesons to create the $\bar{\nu}_\mu$ dominant beam. The details of the BNB neutrino flux prediction can be found in Ref. [6].

MiniBooNE collected 6.46×10^{20} proton-on-target (POT) in neutrino mode, and 11.27×10^{20} POT in anti-neutrino mode.

2.2 The MiniBooNE detector

The MiniBooNE detector, located 541 m away from the target, is a mineral-oil-based Cherenkov detector. The 12.2 m spherical tank, filled with pure mineral oil, $(CH_2)_n$, has two optically separated regions. The interior region, lined by 1280 8-inch photo-multiplier tubes (PMTs), contains the target volume. An outer volume, equipped with 240 8-inch PMTs, serves as the veto region [7]. The presence of a charged particle above threshold is detected through the Cherenkov radiation observed by PMTs. As seen from Figure 1, top right, the inner volume is painted black to prevent scattering of

the Cherenkov light, improving the reconstruction precision. On the other hand, the outer volume is painted white to enhance scattering of Cherenkov light, in order to achieve the 99.9% rejection of cosmic rays by the veto [8] even with fairly sparse PMT coverage. The charge and time information from all PMTs is used to reconstruct kinematics of charged-lepton and electromagnetic events. MiniBooNE mineral oil produces a small amount of scintillation light which can be used to reconstruct the total energy of the interaction via calorimetry, which is particularly important for particles below Cherenkov threshold.

For the $\nu_\mu \to \nu_e$ ($\bar{\nu}_\mu \to \bar{\nu}_e$) oscillation study, the following three particle reconstruction algorithms were the most important: single Cherenkov rings from 1) a muon and 2) an electron, and the two-ring electromagnetic shower topology from 3) a neutral pion decay to two gammas. Figure 2 shows the different characteristics of these three signals, including examples of typical events in the detector [4].

The reconstruction algorithms can also reconstruct more complicated topologies important for constraining backgrounds and for cross section studies discussed below. The charged-current single charged pion (CC1π^+) interaction reconstruction algorithm [9] fit two Cherenkov rings from final state particles, a charged lepton and a positive pion, to find their kinematics. The charged-current single neutral pion (CC1π°) interaction reconstruction algorithm [10] fit a charged lepton and a neutral pion (which consists of two electromagnetic showers, *i.e.* the algorithm fits for three Cherenkov rings). Another algorithm identifies and reconstructs the neutral current elastic (NCE) interaction [11], where the total kinetic energy of final state nucleons is found using scintillation light.

Along with reconstruction of the light topology in the detector, event identification also relies upon "subevents." These are bursts of light separated in time which indicate a sequence of decay. For example, a muon which stops and then emits a decay ("Michel") electron will produce two subevents, one from the initial muon and the one from the Michel electron.

3 MiniBooNE cross-section results

All searches for BSM physics rely on a precise understanding of SM interactions. However, when MiniBooNE began running, there was little neutrino cross section data in the 100 MeV to few GeV energy regime. In response, MiniBooNE developed a highly successful campaign of cross section measurements, some of which are described here. These results are interesting by themselves and also can be used as direct inputs to the BSM analyses, as described later in this paper.

MiniBooNE's beam is among the first high-statistics, high purity fluxes in the energy range from 100 to 1500 MeV. The observation of the resulting events in a large, isotropic detector with 4π coverage is unique. Within this detector it is relatively easy to achieve uniform angular acceptance. Also, the active veto makes it possible to measure NC interactions effectively. Insensitivity of hadronic details worked in positively. The hadron multiplicity often causes confusions for tracker detectors. Although the MiniBooNE detector cannot measure multiple hadron tracks, it measures total energy of low energy hadrons (such as protons below Cherenkov threshold from CCQE interactions) in calorimetric way, and, as a result, the details of final state interactions (FSIs), such as re-scattering, absorption, and charge exchange, do not strongly affect reconstruction of kinematics.

Perhaps most importantly to the overall impact of the data, the MiniBooNE collaboration provided the cross section data in a form that is most useful to theorists. Traditionally, cross section data have been presented either as a function of neutrino energy (E_ν) or 4-momentum transfer (Q^2). This presentation is problematic in the MiniBooNE energy region, because of the importance of nuclear

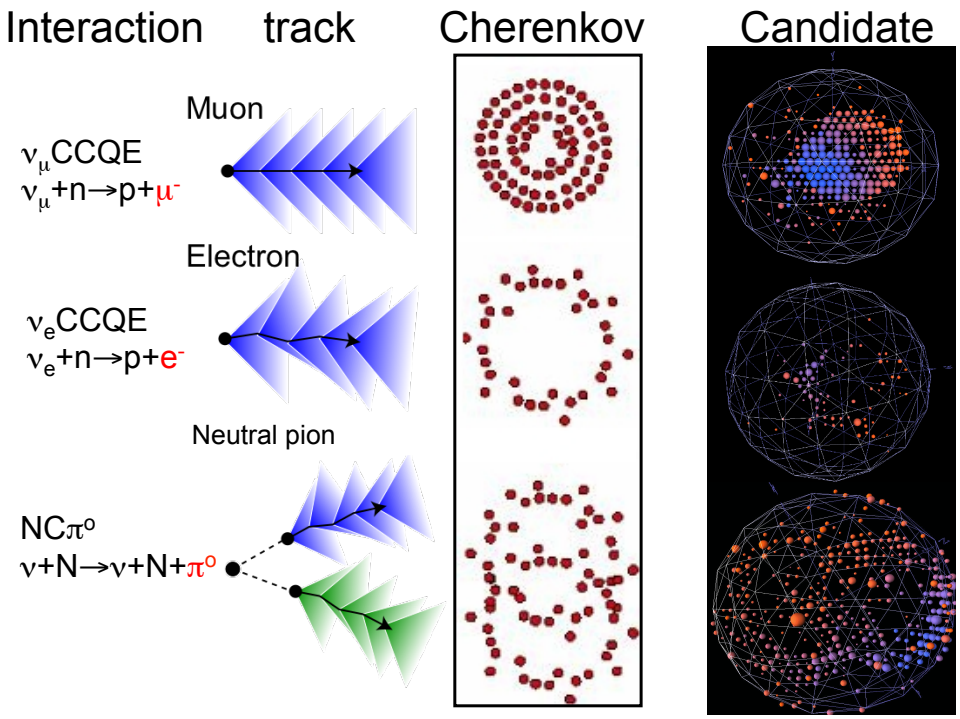

Figure 2: (color online) MiniBooNE particle reconstruction [4]. From top to bottom, a muon neutrino charged-current quasi-elastic (CCQE) interaction, an electron neutrino CCQE interaction, and a neutral current, neutral pion production (NC1π°) interaction. The second and the third columns show the characteristics of tracks and Cherenkov rings [8], and the last column shows the event displays of candidate events.

effects: Fermi motion smears the kinematics, binding energy shifts the energy spectrum, nucleon correlations affect both energy dependence and normalization of cross sections, pions may be created, absorbed, and charge-exchanged within the nuclear environment. These nuclear processes modify the features of primary neutrino-nucleon interactions, and so model dependent corrections are required to reconstruct E_ν and Q^2. This model dependence is problematic because there are a wide range of models available [12–16].

Instead, MiniBooNE chose to publish flux-integrated differential cross sections in terms of measured kinematic variables, which are essentially model-independent. These results have the detector efficiency unfolded but are presented without any others corrections. In particular, the neutrino flux is not unfolded. The result is data that is neutrino-beam specific, and theoretical models are comparable only if those models are convoluted with the MiniBooNE predicted neutrino flux. However, this is trivial for all theorists to do, given that MiniBooNE published a first-principles flux prediction [17]. This isolates all model dependence in the data-to-prediction comparison entirely to the "prediction" side of the discussion. The data remains completely general. For this reason, the MiniBooNE cross section data are widely used to study and compare theoretical models. In this section, we describe each cross section measurement briefly.

3.1 Charged-Current Quasi-elastic (CCQE) scattering

The CCQE interaction is the primary interaction at MiniBooNE energies. This interaction is used to detect ν_μ ($\bar{\nu}_\mu$) and $\nu_e(\bar{\nu}_e)$ candidate events in the oscillation and Lorentz violation analyses,

$$\nu_\mu + n \to \mu^- + p \quad , \quad \bar{\nu}_\mu + p \to \mu^+ + n \ ,$$
$$\nu_e + n \to e^- + p \quad , \quad \bar{\nu}_e + p \to e^+ + n \ .$$

Therefore, a strong understanding of this channel is essential. High statistics ν_μ ($\bar{\nu}_\mu$) interactions are used to study outgoing lepton kinematics [18]. The observable of this channel is the outgoing muon, with no pions in the final state, *i.e.*, the signal event topology is "1 muon + 0 pion + N protons". The main results were published in terms of flux-integrated double differential cross sections, as functions of the lepton kinetic energy and the scattering angle. Figure 3 left shows the flux-integrated double differential cross section of ν_μCCQE interactions [5]. The irreducible background from the pion production channel is subtracted based on a sideband study, but the subtracted background is also published so that readers can recover the irreducible background.

These data have revealed the importance of nucleon correlations [19, 20] in neutrino scattering, which had not been taken into account correctly in previous calculations. This led to models developed using electron scattering data, that were tested against MiniBooNE data [21–26]. These models await being tested further by other experiments, such as MINERvA [27, 28] and T2K [29].

Another important test is CCQE anti-neutrino scattering, where a wide range of expectations were predicted prior to the run [30–34]. Before the data could be compared to the results, however, the substantial contamination of neutrinos in the anti-neutrino beam had to be addressed. Three independent methods were used to constrain and tune the neutrino contamination prediction [35]. After subtracting the neutrino contamination, the flux-integrated double differential cross section for the muon anti-neutrino CCQE interaction was measured (Fig. 3, right) [36]. The comparison of models with data showed a preference for the high cross section models [37]. The rich shape information of the double differential data continues to provide additional tests, beyond the normalization.

The main result of the $\bar{\nu}_\mu$ CCQE cross section measurements is quoted as per CH_2 molecule. This is because the MiniBooNE target consists of CH_2, and the experiment cannot distinguish anti-neutrino interactions with bound protons in the carbon nuclei and free protons from hydrogen. As a separate study, however, MiniBooNE also presented an analysis that subtracted the hydrogen interactions, where the cross sections were then expressed per bound proton. This has also provided a useful handle for theorists.

3.2 Charged single pion production

The understanding of charged-current single-pion channels is of great interest to the nuclear community, but also, there are significant implications for the neutrino oscillation studies. These interactions produce an irreducible background for CCQE events [38–41]. If the detector fails to tag outgoing pions, either because of detector effects or nuclear effects, pion production channels may be misclassified as CCQE. The distributions of irreducible backgrounds must be modelled, and those models rely on the pion production measurements, especially the MiniBooNE data described here. Therefore, understanding the kinematic distributions of pion production channels is a crucial task for neutrino oscillation physics.

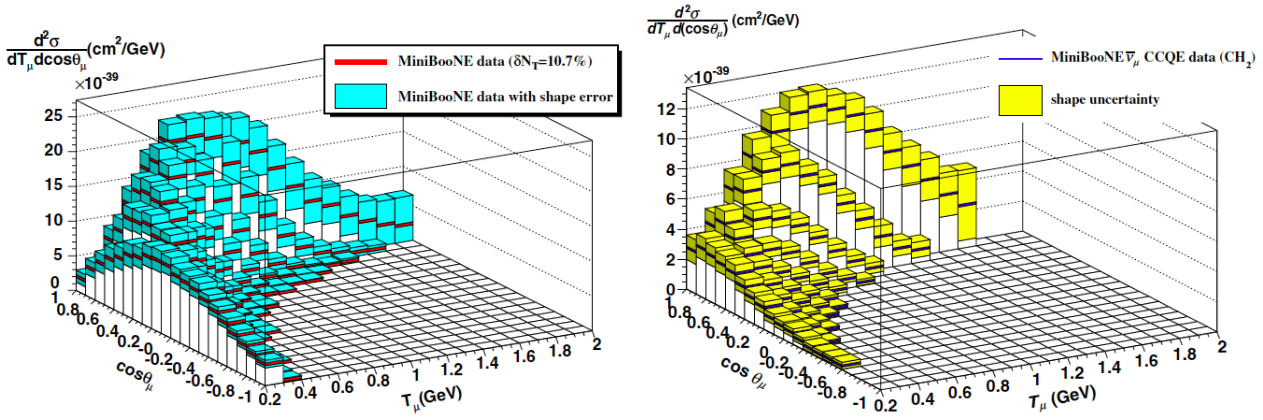

Figure 3: (color online) MiniBooNE CCQE cross sections. The left plot shows the muon neutrino flux-integrated CCQE double differential cross section on a neutron target. The right plot shows muon anti-neutrino flux integrated CCQE double differential cross section on a CH_2 molecule.

There are three pion production channels for which MiniBooNE performed dedicated measurements: charged-current single π^+ (CC1π^+) production [9]; charged-current single π° (CC1π°) production [10]; and neutral current single π° (NC1π°) production [42].

$$\begin{aligned} \nu_\mu + CH_2 &\rightarrow \mu^- + \pi^+ + X \ , \\ \nu_\mu + CH_2 &\rightarrow \mu^- + \pi^\circ + X \ , \\ \nu_\mu(\bar{\nu}_\mu) + CH_2 + &\rightarrow \nu_\mu(\bar{\nu}_\mu) + \pi^\circ + X \ . \end{aligned}$$

Here, the topologies of each event are more complicated and are described as "1 muon + 1 positive pion + N protons" (CC1π^+), "1 muon + 1 neutral pion + N protons" (CC1π°), and "0 muon + 1 neutral pion + N protons" (NC1π°). Although the MiniBooNE detector is not magnetized and therefore cannot distinguish positive and negative pions based on their trajectories, separation is possible. Negative pions are absorbed by a nucleus almost 100% of the time, and in consequence, there is no emission of a Michel electron. This fact allows MiniBooNE to use the presence of a Michel electron to select positive pions.

Because of the more complicated topologies, the differential cross sections for these data sets are presented in various variables. Among them, distributions in pion kinetic energy and momentum distributions exhibit the presence of nuclear effects, while we do not see this from the lepton distributions. Figure 4 shows differential cross sections, CC1π^+ pion kinetic energy and CC1π° pion momentum, respectively. The shape and normalization are sensitive to nuclear effects, such as pion absorption, charge exchange, and rescattering. Therefore, the state-of-the-art nuclear models [43, 44] can be tested by these MiniBooNE data.

3.3 Neutral-Current Elastic (NCE) scattering

The NCE interaction can take place on both neutrons and protons, for both neutrino and anti-neutrinos. The results are relevant for dark matter searches in two ways: first through the measurement

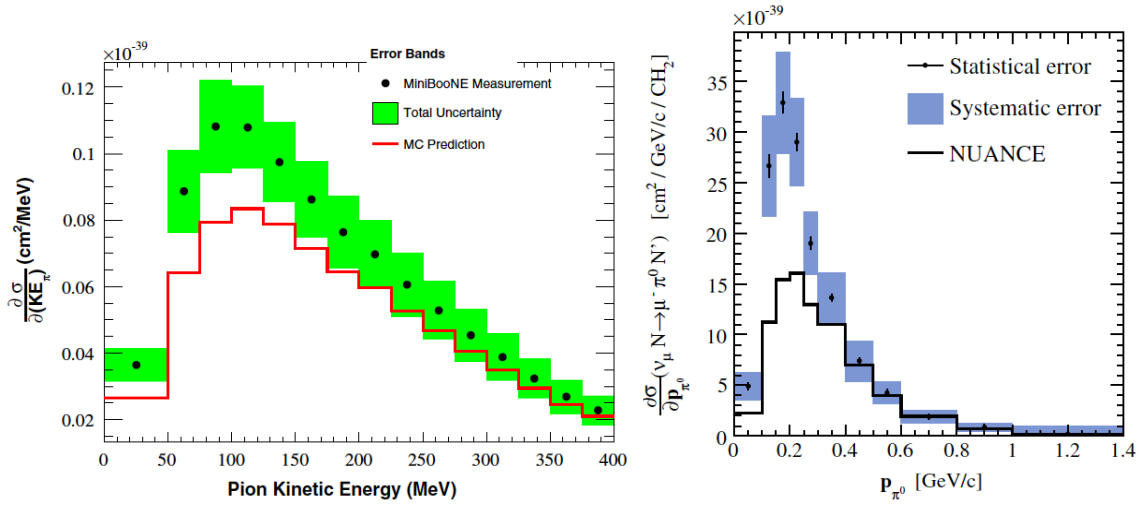

Figure 4: (color online) MiniBooNE single pion production results. The left plot is π^+ kinetic energy differential cross section from CC1π^+ interaction on CH_2 [9]. The right plot is π° momentum differential cross section from CC1π° interaction in CH_2 [10]. As you see, predictions underestimate data for both channels and the shapes do not agree as well.

of Δs that we describe here; second as a background to a direct dark matter search by MiniBooNE, described in sec. 6.

$$\begin{aligned} \nu_\mu(\bar{\nu}_\mu) + p &\rightarrow \nu_\mu(\bar{\nu}_\mu) + p \ , \\ \nu_\mu(\bar{\nu}_\mu) + n &\rightarrow \nu_\mu(\bar{\nu}_\mu) + n \ . \end{aligned}$$

Since only protons with kinetic energy above ∼350 MeV produce Cherenkov radiation (Fig. 5, left), the majority of these events only produce scintillation light, and therefore necessitate a strictly calorimetric analysis. We call this topology "0 muon + 0 pion + N protons". However, when the kinetic energy exceeded the Cherenkov threshold, it is also possible to observe the direction of nucleons [11].

The calorimetric measurement causes the signal to be insensitive to the detailed final state interaction (FSI) process. Also, similar to the anti-neutrino CCQE analysis (Sec. 3.1), scattering on C and H cannot be distinguished, so the target may be a bound proton, a free proton, or a bound neutron. Hence, the cross section is presented per CH_2 target. Figure 5, right, shows the anti-neutrino mode NCE differential cross section [45].

The NCE data allows us to refine our understanding of nuclear effects at low Q^2. In NCE, the observable is the sum of all kinetic energies of out going protons, $\sum T_N$. Using this, the Q^2 can be reconstructed by assuming the target nucleon at rest,

$$Q^2_{QE} = 2M_N \sum T_N \tag{2}$$

Note that irreducible backgrounds, such as NC pion production without an outgoing pion, are subtracted to make Q^2_{QE} physical.

The reconstructed data shows a roll-over at the low Q^2 region, due to the combination of Pauli blocking and the nuclear shadowing. Pauli blocking is a phenomena where low momentum transfer

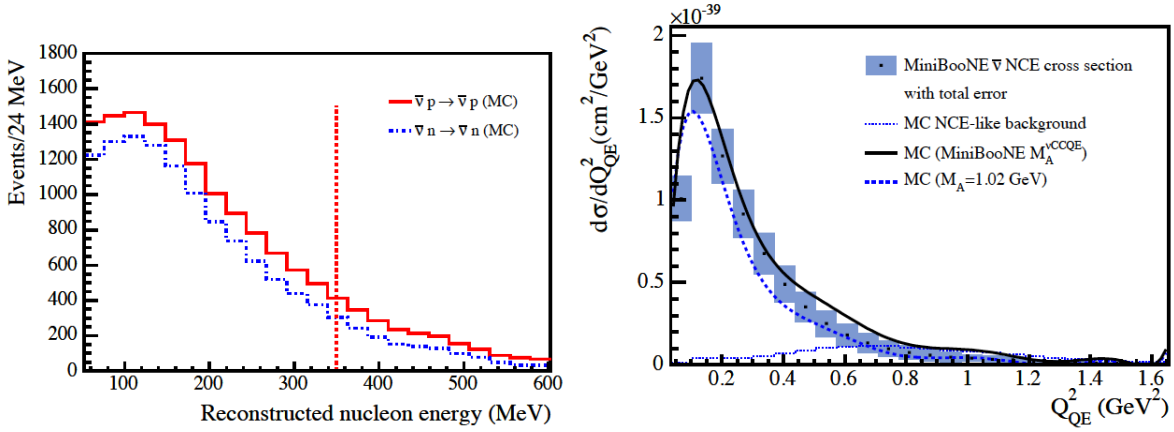

Figure 5: (color online) MiniBooNE NCE results [45]. The left plot shows simulated kinetic energy of protons and neutrons from NCE in MiniBooNE. The line denotes the Cherenkov threshold, *i.e.*, only protons which have higher energy from this line emit Cherenkov radiation. For neutrons, there is no Cherenkov radiation and the chance the secondary proton from the primary neutron exceeds this threshold is extremely low (in other words, if the proton exceeds Cherenkov threshold, this will most likely form the primary neutrino NC interaction). The right plot shows the anti-neutrino NCE differential cross section. As you see, the data shows a "roll-over" in the low Q^2 region.

interactions are forbidden due to occupied phase space, and the nuclear shadowing happens when the resolution (=low momentum transfer interaction) is insufficient to resolve a single nucleon wave function. Note that these nuclear effects do not appear if the signal of NCE is defined to be a single isolated proton, where strong FSI migrates all nucleons to low energy region [46]. However, because the MiniBooNE NCE data presents the sum of the total nucleon kinetic energy, the results preserve the feature of the primary neutrino interaction physics.

NCE interactions are connected to direct dark matter searches through the measurement of Δs , the spin of the strange quarks in the nucleon. It has been shown [47] that the uncertainty of Δs on the spin-dependent scattering between dark matter particles and target nuclei can be a large systematic error. Therefore, a Δs measurement is another way that neutrino cross section measurements contribute to BSM physics. We briefly consider how this information can extracted from the NCE data here.

The spin structure of a nucleon is deeply fundamental and quite complicated. In the naive constituent quark model, the spin-$\frac{1}{2}$ of a nucleon can be derived by adding valence quark spins, where in the static limit ($Q^2 \to 0$) there are three valence quarks that make up all static properties of a nucleon, such as charge, magnetic moment, and spin. However, the spin contribution from up and down quarks deduced from inclusive deep inelastic scattering (DIS) measurements [48–50] indicate, in the static limit, that up and down quarks support only ∼10% of the total spin of a proton. This so-called "spin crisis" has triggered a world wide effort to look for other sources of spin in a nucleon. One of the interesting additional spin contributions is from the strange quarks, called Δs. Although recent measurements show the static limits of the strange quark charge and magnetic contributions are consistent with zero [51], the nonzero value of Δs is still under debate [52], because the weak coupling ($\propto (1 - 4sin^2\theta_w)$) of Δs with parity violating electron asymmetry does not allow a clear measurement

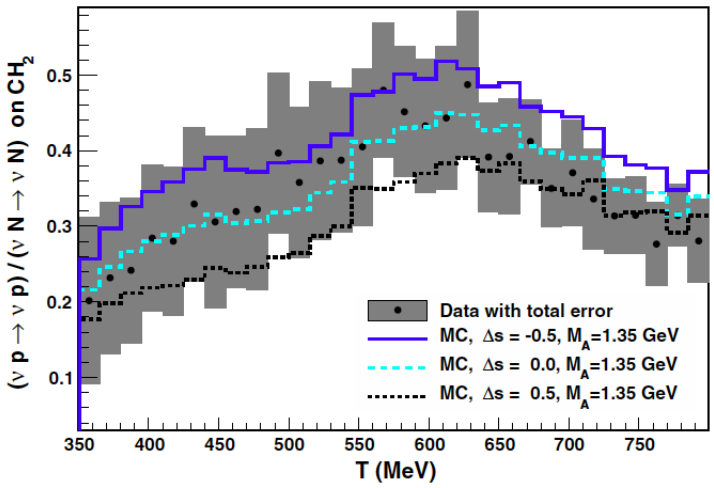

Figure 6: (color online) The MiniBooNE Δs fit result [11]. The contribution of Δs increases the proton NCE cross section, and decreases the neutron NCE cross section. Therefore, it is necessary to separate proton and neutron NCE, which is possible for the high energy sample. Here, the denominator is chosen to be the total NCE events ($\nu + N \to \nu + N$) in order to cancel systematics. However, the large systematic errors do not allow MiniBooNE to definitively measure a nonzero Δs contribution.

of Δs through electron scattering experiments.

However, Δs also contributes to neutrino NCE scattering, as an axial vector isoscalar term, increasing the cross section for neutrino-proton NCE, and decreasing the cross section for neutrino-neutron NCE. MiniBooNE can only isolate neutrino-proton NCE in the case of high energy protons. Fig. 6 shows the fit result of neutrino NCE data. The best fit value is $\Delta s = 0.08 \pm 0.26$. Unfortunately, MiniBooNE does not have enough sensitivity to definitively determine nonzero Δs. This is due to the poor experimental proton-neutron separation which is only possible at high energy with large systematics. Therefore, a detector which has the ability to identify low energy protons, such as MicroBooNE [53], will have better sensitivity to Δs.

4 MiniBooNE oscillation results

The most well-known BSM search performed by the MiniBooNE experiment was for neutrino oscillations consistent with LSND. These are also the most thoroughly reviewed results. Here, we briefly describe the studies. We recommend Ref. [54] for a more extended discussion.

MiniBooNE was conceived in 1998, shortly after the LSND results had reached 3.8σ significance and before the three massive neutrino model for active-flavor oscillations (νSM) had been well-established. However, it was clear that if LSND was observing an oscillation signal, the associated squared mass splitting (Δm^2_{large}) was more than an order of magnitude larger than other evidence for oscillations. In this circumstance, a complicated three-neutrino appearance probability can reduce to a more simple two neutrino case for designs with $(1.27L/E) \approx 1/\Delta m^2_{large}$, such as MiniBooNE.

This approach assumes no CP violation in the mixing matrix, and hence equal probabilities of neutrino and anti-neutrino oscillations. Leptonic CP violation in the mixing matrix had been discussed

by Wolfenstein in 1978 [55] as a natural analogy to the quark sector. However, by extension of that analogy, the assumption was that this effect, if it existed, would be very small. As a result, theoretical interest in 1998 was largely isolated to CP violation. In retrospect, this approach was naive, but this made sense as the guiding principle for the MiniBooNE design at the time. The goal was to test a simple two-neutrino oscillation model with equal probabilities of neutrinos and anti-neutrinos, on the basis that this would be a good approximation if the underlying reality was BSM physics. If a signal was not observed, the significantly different systematic errors were expected to result in a clear exclusion of the result. Thus, the MiniBooNE experiment began running in neutrino mode, which provided roughly ∼6 times higher rate than anti-neutrino mode–a necessary choice since the MiniBooNE experiment was also relied on a significant Booster performance improvement. The results showed an anomalous excess of electron like events in the ν_μ dominant neutrino mode beam [56] that was similar to, but not in good agreement with, LSND. The experiment then switched to running in anti-neutrino mode, where a result in agreement with LSND was observed.

Rather than consider these events historically, we present both results together in the next section, followed by a discussion of interpretations and considerations of follow-up experiments. There is a world-wide effort to probe the sterile neutrino in the region $\Delta m^2 \sim 1$ eV^2 [57]. It is desirable for MiniBooNE to confirm this excess is electron-like, which is considered the sterile neutrino oscillation signal, not background gamma rays associated with $\nu_\mu(\bar{\nu}_\mu)$NC interactions. The MicroBooNE experiment [53] was proposed along this line. The MicroBooNE experiment features a large liquid argon (LAr) time projection chamber (TPC), and it has an ability to distinguish an electron (positron) and a gamma ray. The MicroBooNE experiment will start data taking in 2014. We will discuss more in a later section.

4.1 The Neutrino and Anti-Neutrino Appearance Oscillation Results

After a decade of data collection, MiniBooNE's final appearance oscillation results have been published [58]. Figure 7 shows the electron candidate ($\nu_\mu \to \nu_e$ oscillation candidate) distribution in neutrino mode and positron ($\bar{\nu}_\mu \to \bar{\nu}_e$ oscillation candidate) distribution in anti-neutrino mode. Note that since the MiniBooNE detector is not magnetized, in general it cannot distinguish between electrons and positrons, and so both are grouped into the "electron-like" category.

MiniBooNE observed event excesses in both modes of running, but the results have slight qualitative difference. In neutrino mode (left bottom plot), there is a statistically significant (3.8σ) event excess in the low energy region. Although the excess is significant, the shape of the spectrum leaves some tension with the oscillation hypothesis from LSND, which you can see from the right bottom plot where the MiniBooNE best fit region does not overlap well with the LSND best fit region. MiniBooNE uses a likelihood-ratio technique [59], to find the best fit values $(\Delta m^2, \sin^2 2\theta) = (3.14\ \text{eV}^2, 0.002)$ in neutrino mode, with χ^2/dof of 13.2/6.8. In anti-neutrino mode (left top plot), the observed excess is not as statistically strong as neutrino mode (2.8σ). This is expected when one compares the protons on target in each mode and considers the lower anti-neutrino flux and cross section. Although the statistical significance is lower, then shape agreement with the LSND hypothesis is better. Again this can be seen from the right top plot where the parameter space selected by the MiniBooNE data agree with the LSND best fit region. The best fit point in this mode was (0.05 eV^2, 0.842) with χ^2/dof of 4.8/6.9.

The combined result significance is dominated by neutrino mode and is 3.8σ. It is possible to find compatible regions in a simple two-neutrino model between the two data sets [58]. However, we

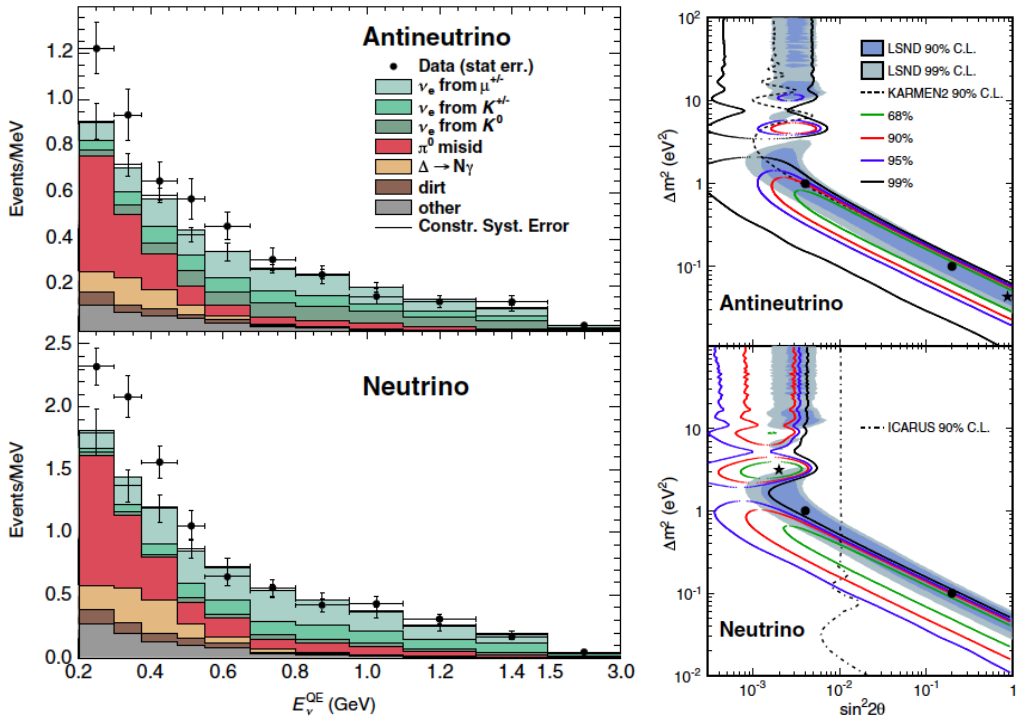

Figure 7: (color online) The final MiniBooNE oscillation results [58]. The left plot shows the reconstructed neutrino energy distribution of oscillation candidate events. The top is for anti-neutrino mode and the bottom is for neutrino mode. Both modes show excesses in the low energy region, while the neutrino mode has higher statistical significance. The right plot shows the allowed region in Δm^2-$sin^2 2\theta$, where the best fit points are shown in black stars. The compatibility with the LSND signal is better in anti-neutrino mode.

emphasize that considering MiniBooNE oscillations in the absence of other oscillation experiments lead to misunderstandings. We consider this point in a later section.

4.1.1 Potential Non-oscillation Explanations

The background-only χ^2-probability for the MiniBooNE oscillation search was 1.6% and 0.5% relative to the best oscillation fits for neutrino and anti-neutrino mode, respectively. Nevertheless, it is important to explore in detail the potential SM explanations of the MiniBooNE results. In particular, a Cherenkov detector, such as MiniBooNE, lacks the ability to distinguish electrons from single photons. Therefore any single photon production mechanism via neutral current interactions is a likely suspect as a background to this search.

The primary source of single photons is the NC1π° reaction, followed by $\pi^0 \rightarrow \gamma\gamma$, where one photon is lost because it exits the detector or because the relativistic boost causes the energy to be too low to allow the Cherenkov signal to be identified. At the low energies of MiniBooNE, the background from two π° rings that merge is less important than the case where a photon is lost. Fortunately, MiniBooNE has the largest sample of well reconstructed NCπ° events ever obtained.

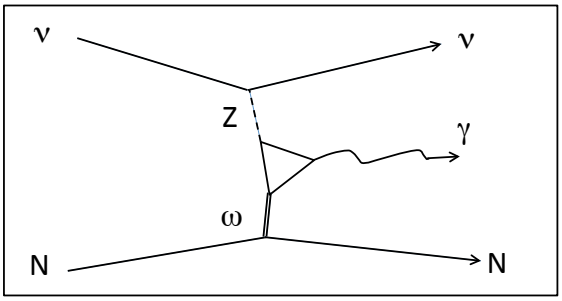

Figure 8: The triangular anomaly mediated photon production. The neutrino neutral current couples via Z-boson, and the target nucleon or nucleus couples with a strong force mediated vector meson, such as an omega meson.

Keeping in mind that the largest uncertainties are in the production and not in the kinematics of the photons themselves, MiniBooNE was able to use this large data set to carefully evaluate this appearance background [60]. This study can constrain the variation of this largest misID background (red histogram in Fig. 7, left), and we have shown that if NCπ° was the source of the MiniBooNE excess, MiniBooNE's systematic error on the production would have to be underestimated by an order of magnitude [56]. This is not a likely solution to the problem, and so we turn to single photon production.

MiniBooNE also included the NC single photon process in their simulation. The process involves the single photon decay of a neutral current Δ resonance, which has a small but non-negligible branching ratio (<1% of NC1π°). The rate of this process is strongly tied to the resonant production of pions, therefore MiniBooNE can utilize their *in situ* NC1π° measurement to constrain this background. Therefore the variation of this second biggest misID background (light brown histograms in Fig. 7, left) is also constrained by the NC1π° measurement, and we found this process was not large enough to explain the MiniBooNE excess [56].

After the first MiniBooNE oscillation result in 2007 [8], it was pointed out that there were additional single-photon-production channels missing from the NUANCE [12] event simulation used by experiments such as MiniBooNE [61]. Figure 8 shows the relevant underlying diagram. This source, triangular anomaly mediated photon production, features weak coupling via the neutrino neutral current, and strong coupling with nucleons or nuclei. In fact, a similar type of interaction was suggested originally in the 1980's [62], however, it was not widely noted or further investigated. This type of process can generate a single gamma ray from a NC interaction. The strength of the anomaly mediated diagram was evaluated [63], and the event rate in MiniBooNE, after convoluting the BNB neutrino flux, was, at the time, estimated to be high enough to explain a part of the MiniBooNE excesses [64].

The initially high estimate, which may have explained the MiniBooNE result, led nuclear theorists to re-evaluate this exotic "$Z-\gamma-\omega$ coupling," properly including nuclear effects, such as Pauli blocking and Δ resonance media width modification, as well as including careful calibrations of nuclear

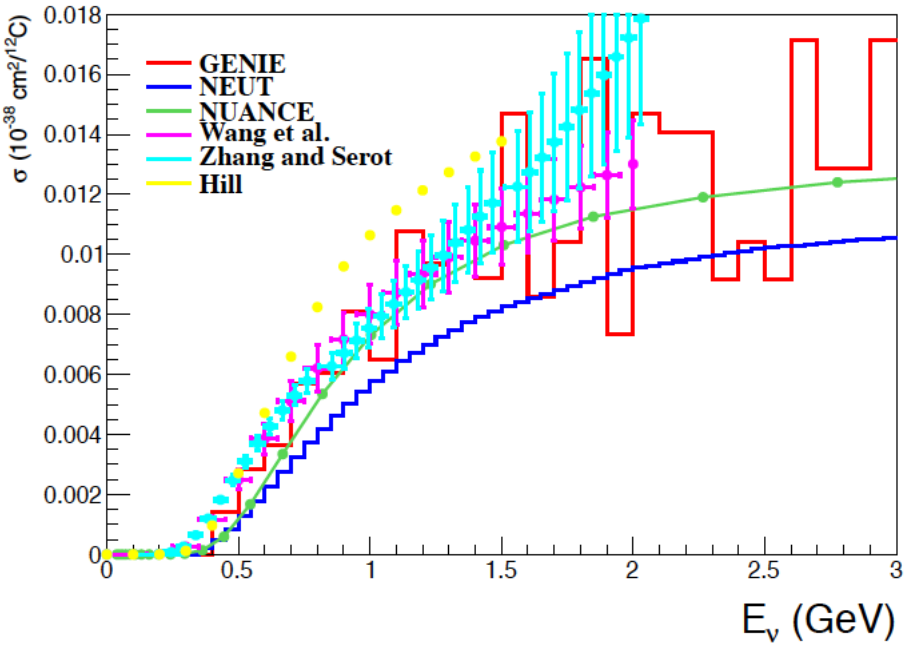

Figure 9: (color online) A comparison of the total cross section of NC photon production per ^{12}C nucleus [68]. The neutrino interaction generators used by experimentalists (GENIE [14], NEUT [15], and NUANCE [12]) tend to predict lower cross sections than state-of-the-art theoretical models (Wang *et al.* [65], Zhang and Serot [69], Hill [64]).

parameters from external data [65–67]. These are important to include since nuclear effects are sizable in this energy region. Note these nuclear effects tend to reduce the cross section.

Figure 9 shows our current knowledge of this channel [68]. The figure shows the total cross section of NC single photon production process per ^{12}C nucleus, which means the cross section includes all potential processes contributing to this final state topology ("0 muon + 0 pion + 1 photon + N protons"), both incoherently (neutrino-nucleon interaction) and coherently (neutrino-nucleus interaction). As you see, all neutrino interaction generators used by experimentalists (GENIE [14], NEUT [15], and NUANCE [12]) tend to predict lower cross sections than state-of-the-art theoretical models by Wang *et al.* [65], Zhang and Serot [69], and Hill [64].

The NC single photon prediction may explain part of the excess, but it is not likely to explain all of it. There was an active discussion on this channel at the recent INT workshop, and further experimental data can help to guide more theoretical work [70].

Meanwhile, a BSM NC single photon model was proposed [71] where a decay of a heavy neutrino produces a single photon signal in the detector. Figure 10 shows the concept of such a model. The heavy neutrino is produced by the mixing with a muon neutrino, then the decay of the heavy neutrino leaves a photon signal in the detector. Interestingly, the required mass range of the heavy neutrino to produce such a signal in the MiniBooNE detector (40 MeV $< m_h <$ 80 MeV) is not constrained by other experiments. The beauty of this model is that it also explains the LSND signal, while evading the KARMEN null oscillation result [72].

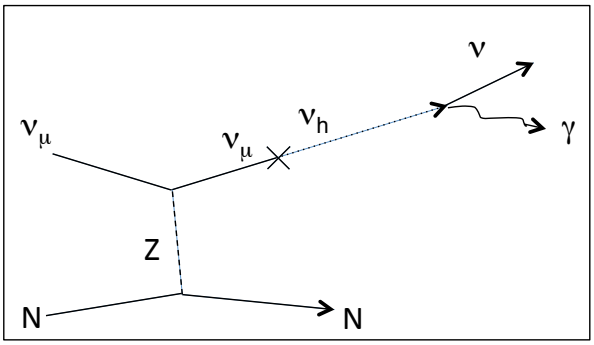

Figure 10: The concept of a heavy neutrino decay signal in the MiniBooNE detector [72]. The mixing of a neutrino with a hypothetical heavy neutrino and its short life time allows for it to decay in the MiniBooNE detector to leave a photon signal.

At this time, NOMAD is the only experiment to have performed a dedicated NC single photon search [73]. The NOMAD result was consistent with their background prediction, thus, NOMAD set a limit on this channel. However, the limit was quoted with NOMAD's average energy ($< E > \sim 17\, GeV$) and is therefore not as relevant for lower energy experiments, such as MiniBooNE. Therefore, it is essential for new experiments that seeks to check the MiniBooNE results to have an ability to distinguish between electrons and photons, such as MicroBooNE [53].

4.1.2 Potential Oscillation Explanations

Numerous articles have been written on the potential of oscillation models to explain the MiniBooNE signal. In particular, we recommend Ref. [74] as a pedagogical discussion of the issues of fitting the data. We excerpt the results from this reference here.

When MiniBooNE and LSND results are considered within the context of the world's oscillation data, νSM is excluded, because a third mass splitting must be introduced. Because the $Z \to \nu\bar{\nu}$ results from LEP and SLD [1] limit the number of low mass active neutrinos to three, sterile neutrinos are introduced to allow for these data sets. Sterile neutrinos are a consequence of many theories and can evade limits from cosmology, as discussed in Ref. [57] .

If one sterile neutrino is added to the three active neutrinos, then the model is termed (3+1). Two additional sterile neutrinos leads to a (3+2) model and three results in a (3+3) model. The mass states are mixtures of flavor states, and in these models, fits to the data yield mass states that are either mostly active flavors or mostly sterile flavors. The splitting between the mostly active and mostly sterile flavors is large, and the splittings between the active flavors is, comparatively, negligible. So, in sterile neutrino fits, the short-baseline approximation where the mostly active flavors are regarded as degenerate in mass is used. In such a model, 3+1 models are simply two-neutrino models, such as what was initially proposed to explain LSND.

The disagreement between the MiniBooNE neutrino and anti-neutrino data leads to very poor fits for 3+1 models. In order to introduce a difference in the neutrino oscillation probabilities, CP violation must be included in the model. For the term which multiplies the CP-parameter to be significant, there must be two mass splittings that are within less than two orders of magnitude of

each other. This can be accommodated in a 3+2 model.

Since the MiniBooNE and LSND results were published, two new anomalies consistent with high Δm^2 oscillations were brought forward. These are the reactor anomaly [75], which has been interpreted as $\bar{\nu}_e \to \bar{\nu}_s$, and the gallium source anomaly [76] which can be interpreted as $\nu_e \to \nu_s$ [57]. Both anomalies have weaker significance than MiniBooNE and LSND, but they can be combined into a consistent model.

With this said, many experiments have searched for oscillations in the high Δm^2 region and found no evidence of oscillations. Ref [74] describes nine such results. The exclusion limits for electron-flavor disappearance and electron-flavor appearance can be shown to be compatible with the results of the four anomalous measurements. However, when muon-flavor disappearance is included, there is tension between the data sets which leads to low compatibility, except in the 3+3 picture.

4.1.3 Near-future Experiment Addressing the MiniBooNE Results

The MicroBooNE experiment is a large liquid argon time projection chamber (LArTPC) experiment [53]. It is part of the US LArTPC program [77], with the eventual goal of an ultra-large LArTPC experiment, such as LBNE [78]. The experiments are motivated by the "bubble chamber level" LArTPC imaging quality.

Figure 11 shows a drawing [53] of MicroBooNE's 170 ton foam-insulated cryostat. The TPC volume is 89 tons. Ionized electrons along the neutrino-induced charged particle tracks are drifted via a high electric field in the TPC volume to the anode wires. The node wires are configured on three planes alternating by 60° orientation, to allow 3-dimensional reconstruction of the tracks. The first 2 wire planes record the signal from the induction on wires, and the last plane records the actual collection of ionization electrons.

An array of 8-inch PMTs is equipped behind the wire planes [79]. The main purpose of this photon collection system is to reject out-of-time cosmic rays and to trigger on in-time signals, since the scintillation light from the interaction arrives in ∼ns whereas the time scale of ionization electron drift is of order ∼ms. The detection of scintillation photons from LAr is not straightforward. First of all, the wavelength of Ar scintillation light is 128 nm, which requires careful R&D on potential wavelength shifters for use in LAr [80–82]. Second, the PMTs themselves behave differently in a cryogenic environment as compared to a warm environment, leading to the need for careful characterization [83].

The purity of the liquid argon must be kept very high to allow electrons to drift a long distance. Electro-negative impurities (e.g. water and oxygen molecules) are removed through a custom made filter to achieve $\leq$ ppb level impurity [84, 85]. Such filtering is also effective for removing nitrogen molecules, which don't affect electron drift but do attenuate scintillation light [86].

A high resolution LArTPC detector will be a powerful tool in understanding the MiniBooNE signal, because the detector is expected to have the excellent electron-photon separation. Energetic electrons and photons both produce an electromagnetic shower in a LArTPC. However, the initial $\frac{dE}{dx}$ of a single photon will be twice higher than in the single electron case in the first few centimeters before the track develops into the shower. Due to their high resolution capabilities, LArTPC detectors can distinguish this difference. Moreover, a displaced vertex, in the case of a photon conversion, can be distinguished from a track that is continuous from the vertex, indicative of an electron. The combination of these details can provide high efficiency background rejection for MicroBooNE.

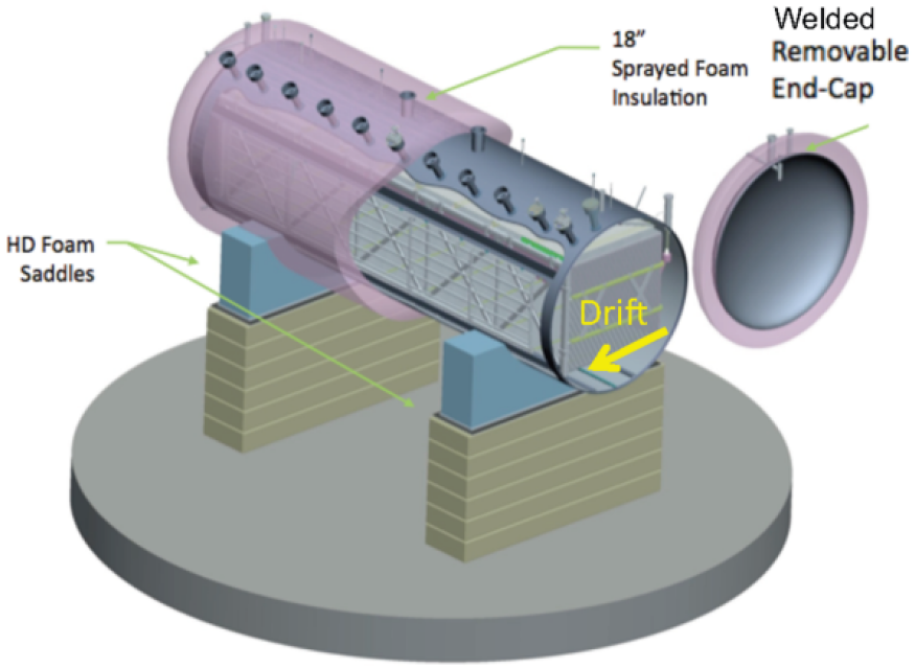

Figure 11: (color online) A drawing of MicroBooNE cryostat [53]. The 170 ton cryostat contains the 89 ton TPC.

5 Test of Lorentz and CPT violation

Lorentz and CPT violation are scenarios motivated from Planck scale theories, such as string theory [87]. In the effective field theory framework, Lorentz violation contributes additional terms to the vacuum Lagrangian of neutrinos, and hence modifies neutrino oscillations [88, 89]. Since Lorentz violating fields are of fixed-direction in the universe, if Lorentz invariance is broken, the rotation of the Earth causes a sidereal time dependence of neutrino oscillation signals. There are number of phenomenological neutrino oscillation models based on Lorentz and CPT violation [90–92], some of which can explain the LSND excess [93]. In fact, a sidereal time dependence analysis of LSND data [94] failed to reject the Lorentz violation scenario. Therefore, it might be possible to reconcile LSND and MiniBooNE oscillation signals under Lorentz violation.

5.1 Analysis

Although Lorentz violation can be studied in any frame or coordinate system, it is convenient to choose one coordinate system to compare data sets. The standard choice is the Sun-centered celestial equatorial coordinates [95], where the origin of the coordinate is the center of the Sun. The orbital plane of the Earth is tilted so that the orbital axis and the rotation axis of the Earth align. This direction define the Z-axis. The X-axis points vernal equinox, and the Y-axis is chosen to complete the right handed system. Because the time scale of the rotation of the galaxy is too long for any

terrestrial experiments, the Sun-centered frame is the better choice to test rotation symmetry (by using the rotation of the Earth) and Lorentz boost (by using the revolution of the Earth).

Having defined the coordinates, one uses the Standard Model-Extension (SME) [96–98] as the framework for a general search for Lorentz violation. The SME can be considered a minimum extension of the SM, including the particle Lorentz and CPT violation. For the neutrino sector, the SME Lagrangian can be written as [88],

$$\mathcal{L} = \frac{1}{2} i \bar{\psi}_A \Gamma^{\mu}_{AB} \overleftrightarrow{D}_{\mu} \psi_B - \bar{\psi}_A M_{AB} \psi_B + h.c., \quad (3)$$

$$\Gamma^{\nu}_{AB} = \gamma^{\nu} \delta_{AB} + c^{\mu\nu}_{AB} \gamma_{\mu} + d^{\mu\nu}_{AB} \gamma_5 \gamma_{\mu} + e^{\nu}_{AB} + i f^{\nu}_{AB} \gamma_5 + \frac{1}{2} g^{\lambda\mu\nu}_{AB} \sigma_{\lambda\mu}, \quad (4)$$

$$M_{AB} = m_{AB} + i m_{5AB} \gamma_5 + a^{\mu}_{AB} \gamma_{\mu} + b^{\mu}_{AB} + \frac{1}{2} H^{\mu\nu}_{AB} \sigma_{\mu\nu}. \quad (5)$$

Here, the AB subscripts represent the flavor basis. The first term of Eq. 4 and the first and second terms of Eq. 5 are the only nonzero terms in the SM, and the rest of the terms are from Lorentz violation.

The physics consequences predicted by Lorentz violation are very rich. Among them, we are interested in Lorentz violating neutrino oscillations, where neutrino oscillations act natural interferometers sensitive to small space-time physics. The smoking gun of Lorentz violation is the sidereal time dependence of physics observables. Therefore, we used the Lorentz violating neutrino oscillation formula [99] to fit the sidereal time distribution of the MiniBooNE oscillation candidate data. Here, potentially, any day-night effect, either from the beam or from the detector, could mimic the sidereal time distribution. MiniBooNE studied effects versus the time distribution of the delivered POT and the high statistics $\nu_{\mu}(\bar{\nu}_{\mu})$ CCQE sample [5, 36], and confirmed that day-night effects on both ν_e and $\bar{\nu}_e$ oscillation candidates are well below statistical errors.

5.2 Results

Figure 12 shows the neutrino and anti-neutrino mode electron-like events as a function of sidereal time [100]. There are three curves fit to the data, depending on different hypotheses. Although the anti-neutrino mode electron-like events show a rather interesting sidereal time dependence, the statistical significance is still low. Therefore, MiniBooNE found that the data are consistent with no Lorentz violation. This analysis provided the first limits on five time independent SME coefficients, at the level of 10^{-20} GeV (CPT-odd) and order 10^{-20} (CPT-even). Further analysis inferred limits on each SME coefficient, and, together with limits from the MINOS near detector [101, 102], it turns out these limits leave tension to reconcile the MiniBooNE and LSND data sets under a simple Lorentz violation motivated scenario [4].

In fact, existing limits from MiniBooNE [100], MINOS [101–104], IceCube [105], and Double Chooz [106, 107] set very tight limits on possible Lorentz violation in the neutrino sector at the terrestrial level. This was one of the reasons why the superluminal neutrino signal from OPERA [108] was suspicious from the beginning. Such a signal would have required very large Lorentz violation, while avoiding all these constraints when writing down the theory. Strictly speaking, this is possible– limits on Lorentz violation from the oscillation experiments cannot be applied directly to the neutrino time of flight (TOF) measurements [109]. However, introducing large Lorentz violation in the neutrino TOF without other large parameters such as those associated with oscillations seems unnatural.

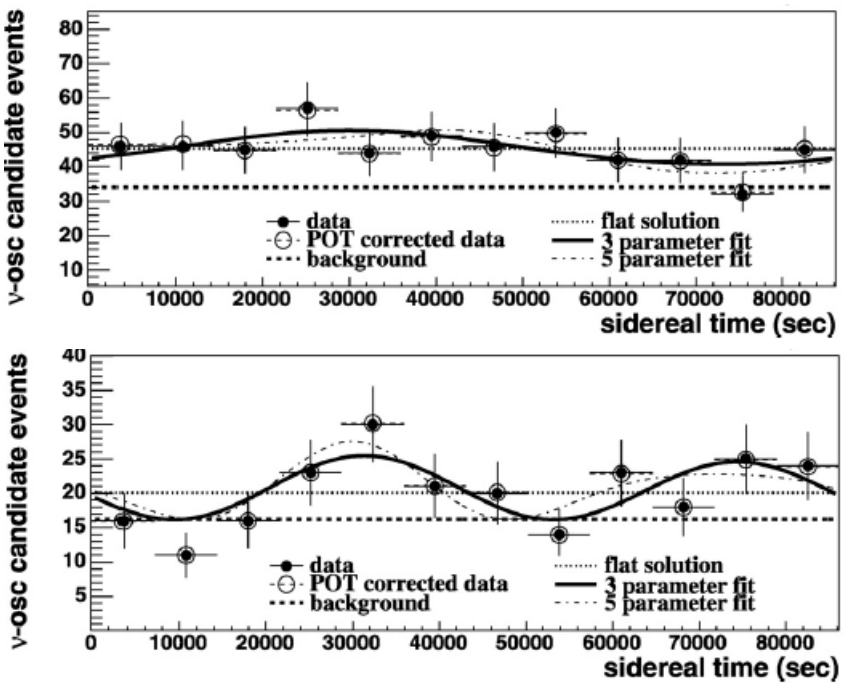

Figure 12: The MiniBooNE Lorentz violation results [100]. The top plot shows the neutrino mode electron-like low energy excess sidereal time distribution, and the bottom plot shows the anti-neutrino mode sidereal time distribution. Here, the data with a POT correction (open circle) show the size of the beam day-night variation. There are three fit curves based on different assumptions, a flat solution (dotted), a three parameter fit (solid curve), and a full five parameter fit (dash-dotted curve).

6 Dark Matter Search

The proton collisions on target in the BNB line that produce a large flux of neutrinos could, potentially, produce sub-GeV scale dark matter particles, that mimic NCE interactions in the MiniBooNE detector [110–112]. The most interesting scenario is that this light dark matter particle is the dark matter of the universe, which requires a light vector mediator particle (called a "dark photon"), in the model in order to obtain an efficient annihilation cross section. The minimum extension of the SM with the light dark matter particle and the vector mediator can be written in the following way [111],

$$\mathcal{L} \;=\; \mathcal{L}_{SM} - \frac{1}{4}V_{\mu\nu}^2 + \frac{1}{2}m_V^2 V_\mu^2 + \kappa V_\nu \partial_\mu F^{\mu\nu} + |D_\mu \chi|^2 - m_\chi^2 |\chi|^2 + \cdots \;. \tag{6}$$

The model has four free parameters: the mass of the light dark matter m_χ, the mass of the vector mediator m_V, kinetic mixing of the vector mediator and the photon κ, and the vector mediator's gauge coupling e' (or $\alpha' = \frac{e'^2}{4\pi}$). Nonzero κ leads to the decay of neutral mesons to a photon and a dark photon, and the dark photon in turn can decay to dark matter particles. This would be the dominant process to produce dark matter particles in the BNB. The second process is direct production from the parton level annihilation by protons colliding in the target.

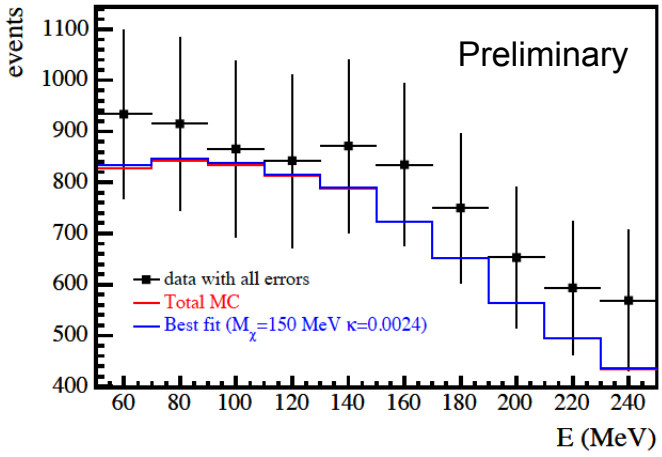

Figure 13: (color online) The dark matter fit result to the NCE data [113]. The plot shows the total energy distribution of the anti-neutrino NCE sample, with a light dark matter hypothesis fit (best fit values, $M_\chi = 150$ MeV and $\kappa = 0.0024$). As can be seen, the current sensitivity to the light dark matter model is low.

6.1 MiniBooNE Searches for Dark Matter particles

MiniBooNE tested this model with the existing anti-neutrino NCE data set, taken during the oscillation studies. Figure 13 shows the fit result with a light dark matter particles hypothesis [113]. The anti-neutrino mode data set is used because it has a lower neutrino interaction rate than the neutrino mode beam. Nevertheless, due to the anti-neutrino backgrounds, only weak limits are obtained on the kinetic mixing parameter κ.

This motivated a tuning of the proton beam that allowed MiniBooNE to run in a mode in which the protons are directed on to the beam dump instead of the target, eliminating the DIF neutrino flux. Figure 14 shows the schematic of this measurement [113]. The beam-dump mode is achieved by tuning the ~1 mm beam to aim 0.9 cm gap between the beryllium target rod and the inner conductor

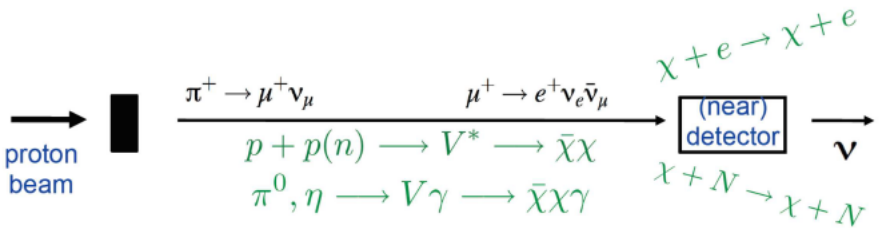

Figure 14: (color online) The concept of the dark matter beam in MiniBooNE [113]. The dominant production mode of dark matter particles are decays of the mediator particles created by decays of neutral mesons. The dark matter particles can be also made through the direct collisions of protons on the beam dump.

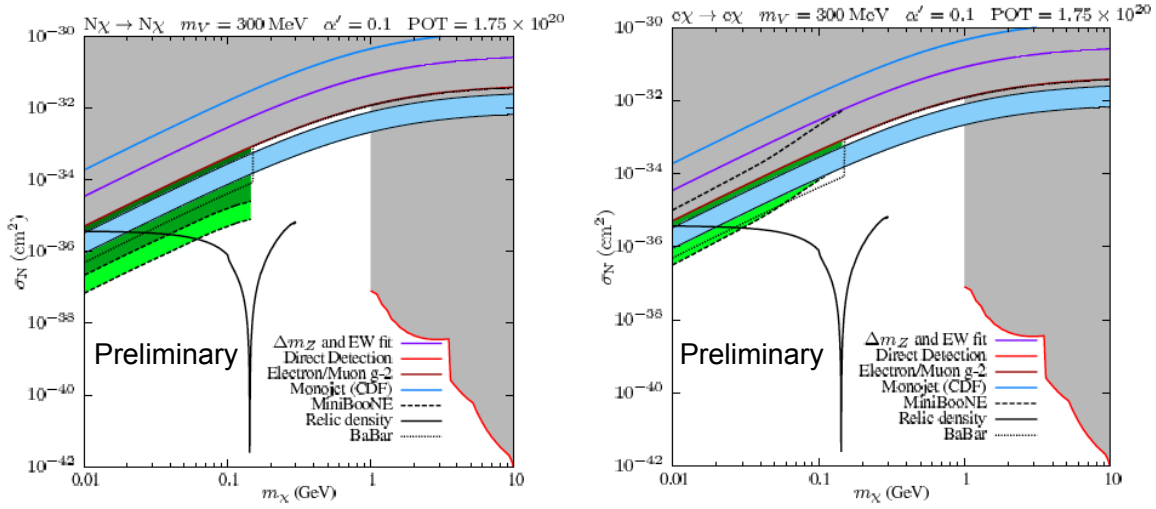

Figure 15: (color online) The MiniBooNE dark matter particles search phase space [113]. Here, the x-axis is the dark matter mass m_χ, and the y-axis is either the dark matter-nucleon or dark matter-electron cross section, assuming the vector mediator mass and the gauge coupling ($m_V = 300$ MeV and $\alpha = 0.1$). The MiniBooNE exclusion region can be seen in green.

of the horn, to hit the beam dump located at the end of decay pipe (50 m from the target) directly. This reduces the neutrino background by roughly a factor of 67. Dark matter production is largely unaffected in this run mode since it occurs through neutral meson decay. MiniBooNE is now running in this configuration. The goal is to accumulate 1.75×10^{20} POT data before MicroBooNE starts beam data taking in the neutrino mode, not the beam-dump mode.

6.2 Parameter space of light dark matter particles and vector mediators

Figure 15 shows the two-dimensional phase space of dark matter-nucleon and dark matter-electron scattering cross sections vs. dark matter mass m_χ [113]. The limits from direct searches end up at the right side ($m_\chi \sim$1 GeV), and the left-side light dark matter region is explored by other techniques, such as rare decays and collider physics. MiniBooNE addresses direct light dark matter searches. In the case of either interaction, MiniBooNE is sensitive to the dark matter mass in the 10 to 200 MeV mass region.

There are many reasons why such a light dark matter search is interesting. First, recent data [114–117] from the direct WIMP (weakly interacting massive particle) searches suggest possible signals of dark matter particles in the lighter mass region. For example, SuperCDMS is also aiming the low mass dark matter search by utilizing the ionization signals [118]. Second, the muon g-2 anomaly can be explained by the presence of a vector mediator [119, 120]. Although the interesting phase space of muon g-2 was already excluded by other experiments, MiniBooNE can further push the limits in this region.

The sensitivity that is obtained from the dark matter-electron scattering looks weaker than dark matter-nucleon in the $\sigma - m_\chi$ phase space (Fig. 15, right), however, as Figure 16 shows, the limit from the dark matter-electron interaction can be stronger in the low vector mass region in $\kappa - m_V$ phase

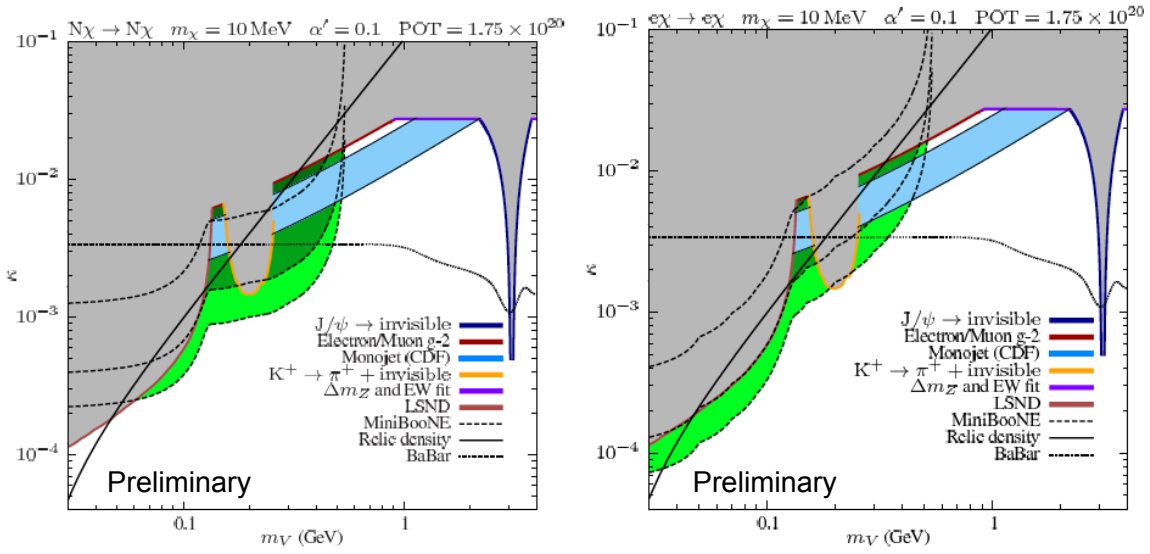

Figure 16: (color online) The MiniBooNE dark matter search phase space [113]. Here, x-axis is the vector mediator mass m_V, and the y-axis is the kinetic mixing parameter κ, assuming the dark matter mass and the gauge coupling ($m_\chi = 10$ MeV and $\alpha = 0.1$). MiniBooNE exclusion region can be seen in green.

space [113]. Therefore, both channels are complimentary and MiniBooNE should strive to measure both. There was a little interest in ν-e elastic scattering because of its small cross section, but this electron channel is as important as the nucleon channel for the dark matter search.

6.3 Dark matter time of flight (TOF)

MiniBooNE's sensitivity to dark matter particles can be further improved by combining event topology and kinematics with the timing information. Figure 17 shows the "dark matter TOF" concept. The dark matter particles are most likely produced at the beam dump after prompt decays of neutral pions or etas ($< 10^{-16}$ sec), so the dark matter production is localized in both time and space. This would result in a dark matter beam that has a well-defined timing, and allows us to perform the TOF-based searches. The heavier dark matter particles should be slower than the neutrinos (as well as the speed of light). Thus the dark matter particles would lag behind the bunch center and separate from the neutrino background.

In the Fermilab Booster, the 81 bunches have 19 ns separations (Sec 2.1). MiniBooNE defines events within 4 ns$< T <$ 16 ns from the bunch center as the in-time events, and the $T <$ 4 ns and $T >$ 16 ns events are out-time. The absolute timing information of all bunches is recorded by the resistive wall monitor (RWM) which is located just before the target. Using the previous MiniBooNE anti-neutrino run to test this idea, Figure 18 shows the overlaid profile of all bunches of anti-neutrino NCE candidate events [113]. As expected, the data shows the peak in in-time, because the data is dominated by anti-neutrino NCE interactions.

A beam dump test run was performed for one week during 2012 running. During the beam-dump

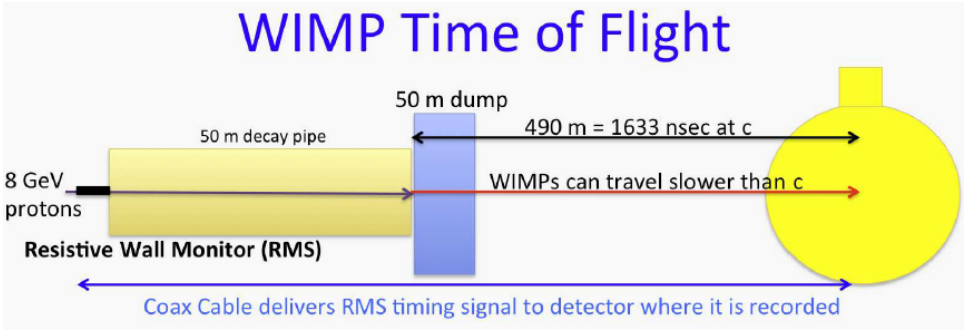

Figure 17: (color online) The concept of dark matter particles TOF. Because of the localization of the dark matter particle production in time and in space, the dark matter beam has well-defined timing structure.

mode test run, the timing of neutrinos was tested using CC interaction. Since the CC interaction is detected through the prompt Cherenkov light from the muons, timing resolution is better than NCE events. Using the new system installed for the beam-dump run, MiniBooNE achieved 1.5 ns resolution [113]. The resolution will be worse for NCE because of the nature of the exponential decay of scintillation light, but MiniBooNE, nevertheless, still expects ∼4 ns resolutions. This gives full confidence for MiniBooNE to perform a full beam-dump run.

7 Conclusion

Since beginning its run in 2002, MiniBooNE has been searching for new physics in a wide variety of ways. The most important results have been those related to oscillations of sterile neutrinos, which has pushed the community toward new and exciting experiments in the future [53, 57, 121–123]. MiniBooNE also tested for possible signals from the Planck scale, *i.e.* Lorentz violation, and set very strong constraints on the SME coefficients. MiniBooNE's light dark matter search with a beam-dump configuration run is a unique opportunity that can provide the best limit on the dark matter mass in the 10 to 200 MeV range. All of these searches have been grounded in the revolutionary set of cross section measurements performed with MiniBooNE. This experiment demonstrates the rich possibilities to go beyond the standard model in low cost short-baseline venues and encourages a strong investment in future programs.

Acknowledgements

JC thanks the National Science Foundation for support through NSF-PHY-1205175. We thank Brian Batell for inputs about light dark matter physics, also we thank Joshua Spitz for careful reading of the manuscript and valuable comments.

References

[1] [Particle Data Group collaboration], J. Beringer *et al.*, Phys. Rev. D **86**:010001 (2012).

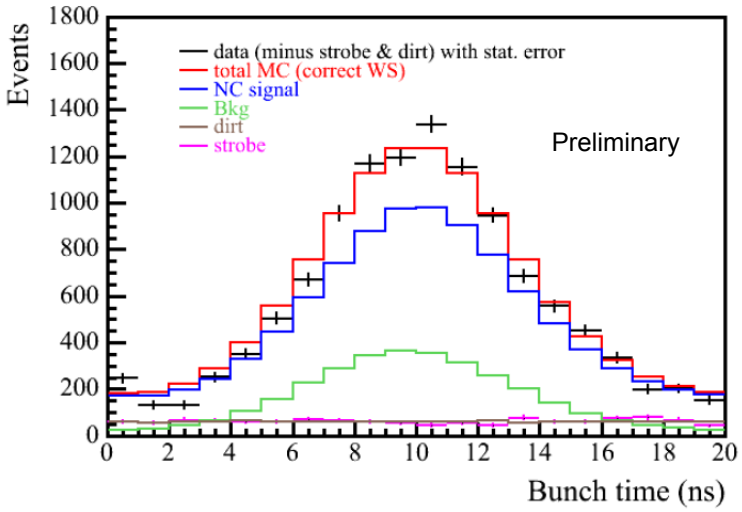

Figure 18: (color online) The reconstructed NCE event time profile for the anti-neutrino mode beam. The events are overlaid relative to the bunch center. As expected, the data peaks in the bunch center, which means these are dominated with anti-neutrino interactions and there is no delay of events.

[2] [T2K collaboration], K. Abe *et al.*, Phys.Rev.Lett. **112**:061802 (2014). [arXiv:1311.4750]

[3] [LSND collaboration], A. Aguilar-Arevalo *et al.*, Phys.Rev. **D64**:112007 (2001). [arXiv:hep-ex/0104049]

[4] [MiniBooNE collaboration], T. Katori, Mod.Phys.Lett. **A27**:1230024 (2012). [arXiv:1206.6915]

[5] [MiniBooNE collaboration], A. Aguilar-Arevalo *et al.*, Phys.Rev. **D81**:092005 (2010). [arXiv:1002.2680]

[6] [MiniBooNE collaboration], A. Aguilar-Arevalo *et al.*, Phys.Rev. **D79**:072002 (2009). [arXiv:0806.1449]

[7] [MiniBooNE collaboration], A. Aguilar-Arevalo *et al.*, Nucl.Instrum.Meth. **A599**:28–46 (2009). [arXiv:0806.4201]

[8] [MiniBooNE collaboration], A. Aguilar-Arevalo *et al.*, Phys.Rev.Lett. **98**:231801 (2007). [arXiv:0704.1500]

[9] [MiniBooNE collaboration], A. Aguilar-Arevalo *et al.*, Phys.Rev. **D83**:052007 (2011). [arXiv:1011.3572]

[10] [MiniBooNE collaboration], A. Aguilar-Arevalo *et al.*, Phys.Rev. **D83**:052009 (2011). [arXiv:1010.3264]

[11] [MiniBooNE collaboration], A. Aguilar-Arevalo *et al.*, Phys.Rev. **D82**:092005 (2010). [arXiv:1007.4730]

[12] D. Casper, Nucl.Phys.Proc.Suppl. **112**:161–170 (2002). [arXiv:hep-ph/0208030]

[13] C. Juszczak, Acta Phys.Polon. **B40**:2507–2512 (2009). [arXiv:0909.1492]

[14] C. Andreopoulos, A. Bell, D. Bhattacharya, F. Cavanna, J. Dobson, *et al.*, Nucl.Instrum.Meth. **A614**:87–104 (2010). [arXiv:0905.2517]

[15] Y. Hayato, Acta Phys.Polon. **B40**:2477–2489 (2009).

[16] O. Buss, T. Gaitanos, K. Gallmeister, H. van Hees, M. Kaskulov, *et al.*, Phys.Rept. **512**:1–124 (2012). [arXiv:1106.1344]

[17] C. Juszczak, J. T. Sobczyk, and J. Zmuda, Phys.Rev. **C82**:045502 (2010). [arXiv:1007.2195]

[18] [MiniBooNE collaboration], A. Aguilar-Arevalo *et al.*, Phys.Rev.Lett. **100**:032301 (2008). [arXiv:0706.0926]

[19] M. Martini, M. Ericson, G. Chanfray, and J. Marteau, Phys.Rev. **C80**:065501 (2009). [arXiv:0910.2622]

[20] J. Nieves, I. Ruiz Simo, and M. Vicente Vacas, Phys.Rev. **C83**:045501 (2011). [arXiv:1102.2777]

[21] M. Martini, M. Ericson, and G. Chanfray, Phys.Rev. **C84**:055502 (2011). [arXiv:1110.0221]

[22] J. Nieves, I. Ruiz Simo, and M. Vicente Vacas, Phys.Lett. **B707**:72–75 (2012). [arXiv:1106.5374]

[23] J. Amaro, M. Barbaro, J. Caballero, T. Donnelly, and C. Williamson, Phys.Lett. **B696**:151–155 (2011). [arXiv:1010.1708]

[24] A. Bodek, H. Budd, and M. Christy, Eur.Phys.J. **C71**:1726 (2011). [arXiv:1106.0340]

[25] A. Meucci, C. Giusti, and F. D. Pacati, Phys.Rev. **D84**:113003 (2011). [arXiv:1110.3928]

[26] O. Lalakulich, K. Gallmeister, and U. Mosel, Phys.Rev. **C86**:014614 (2012). [arXiv:1203.2935]

[27] [MINERvA collaboration], G. Fiorentini *et al.*, Phys.Rev.Lett. **111**:022502 (2013). [arXiv:1305.2243]

[28] [MINERvA collaboration], L. Fields *et al.*, Phys.Rev.Lett. **111**:022501 (2013). [arXiv:1305.2234]

[29] [T2K collaboration], K. Abe *et al.*, Phys.Rev. **D87**:092003 (2013). [arXiv:1302.4908]

[30] M. Martini, M. Ericson, G. Chanfray, and J. Marteau, Phys.Rev. **C81**:045502 (2010). [arXiv:1002.4538]

[31] M. Martini and M. Ericson, Phys.Rev. **C87**:065501 (2013). [arXiv:1303.7199]

[32] J. Nieves, I. Ruiz Simo, and M. Vicente Vacas, Phys.Lett. **B721**:90–93 (2013). [arXiv:1302.0703]

[33] A. Meucci and C. Giusti, Phys.Rev. **D85**:093002 (2012). [arXiv:1202.4312]

[34] J. Amaro, M. Barbaro, J. Caballero, and T. Donnelly, Phys.Rev.Lett. **108**:152501 (2012). [arXiv:1112.2123]

[35] [MiniBooNE collaboration], A. Aguilar-Arevalo *et al.*, Phys.Rev. **D84**:072005 (2011). [arXiv:1102.1964]

[36] [MiniBooNE collaboration], A. Aguilar-Arevalo *et al.*, Phys.Rev. **D88**:032001 (2013). [arXiv:1301.7067]

[37] [MiniBooNE collaboration], J. Grange and R. Dharmapalan (2013). [arXiv:1304.7395]

[38] M. Martini, M. Ericson, and G. Chanfray, Phys.Rev. **D85**:093012 (2012). [arXiv:1202.4745]

[39] D. Meloni and M. Martini, Phys.Lett. **B716**:186–192 (2012). [arXiv:1203.3335]

[40] J. Nieves, F. Sanchez, I. Ruiz Simo, and M. Vicente Vacas, Phys.Rev. **D85**:113008 (2012). [arXiv:1204.5404]

[41] O. Lalakulich, U. Mosel, and K. Gallmeister, Phys.Rev. **C86**:054606 (2012). [arXiv:1208.3678]

[42] [MiniBooNE collaboration], A. A. Aguilar-Arevalo *et al.*, Phys.Rev. **D81**:013005 (2010). [arXiv:0911.2063]

[43] O. Lalakulich and U. Mosel, Phys.Rev. **C87**:014602 (2013). [arXiv:1210.4717]

[44] E. Hernndez, J. Nieves, and M. J. V. Vacas, Phys.Rev. **D87**:113009 (2013). [arXiv:1304.1320]

[45] [MiniBooNE collaboration], A. Aguilar-Arevalo *et al.* (2013). [arXiv:1309.7257]

[46] T. Leitner, L. Alvarez-Ruso, and U. Mosel, Phys.Rev. **C74**:065502 (2006). [arXiv:nucl-th/0606058]

[47] J. R. Ellis, K. A. Olive, and C. Savage, Phys.Rev. **D77**:065026 (2008). [arXiv:0801.3656]

[48] [European Muon collaboration], J. Ashman *et al.*, Phys.Lett. **B206**:364 (1988).

[49] [Spin Muon Collaboration (SMC) collaboration], D. Adams *et al.*, Phys.Lett. **B329**:399–406 (1994). [arXiv:hep-ph/9404270]

[50] V. Hughes, V. Papavassiliou, R. Piegaia, K. Schuler, and G. Baum, Phys.Lett. **B212**:511–514 (1988).

[51] [G0 collaboration], D. Androic *et al.*, Phys.Rev.Lett. **104**:012001 (2010). [arXiv:0909.5107]

[52] S. F. Pate, D. W. McKee, and V. Papavassiliou, Phys.Rev. **C78**:015207 (2008). [arXiv:0805.2889]

[53] [MicroBooNE collaboration], L. Camilleri, Nucl.Phys.Proc.Suppl. **237-238**:181–183 (2013).

[54] J. M. Conrad, W. C. Louis, and M. H. Shaevitz, Ann.Rev.Nucl.Part.Sci. **63**:45–67 (2013). [arXiv:1306.6494]

[55] L. Wolfenstein, Phys.Rev. **D18**:958–960 (1978).

[56] [MiniBooNE collaboration], A. Aguilar-Arevalo *et al.*, Phys.Rev.Lett. **102**:101802 (2009). [arXiv:0812.2243]

[57] K. Abazajian, M. Acero, S. Agarwalla, A. Aguilar-Arevalo, C. Albright, *et al.* (2012). [arXiv:1204.5379]

[58] [MiniBooNE collaboration], A. Aguilar-Arevalo *et al.*, Phys.Rev.Lett. **110(16)**:161801 (2013). [arXiv:1207.4809]

[59] [MiniBooNE collaboration], A. Aguilar-Arevalo *et al.*, Phys.Rev.Lett. **105**:181801 (2010). [arXiv:1007.1150]

[60] [MiniBooNE collaboration], A. Aguilar-Arevalo *et al.*, Phys.Lett. **B664**:41–46 (2008). [arXiv:0803.3423]

[61] J. A. Harvey, C. T. Hill, and R. J. Hill, Phys.Rev.Lett. **99**:261601 (2007). [arXiv:0708.1281]

[62] S. Gershtein, Y. Y. Komachenko, and M. Y. a. Khlopov, Sov.J.Nucl.Phys. **33**:860 (1981).

[63] R. J. Hill, Phys.Rev. **D81**:013008 (2010). [arXiv:0905.0291]

[64] R. J. Hill, Phys.Rev. **D84**:017501 (2011). [arXiv:1002.4215]

[65] E. Wang, L. Alvarez-Ruso, and J. Nieves, Phys.Rev. **C89**:015503 (2014). [arXiv:1311.2151]

[66] X. Zhang and B. D. Serot, Phys.Rev. **C86**:035504 (2012). [arXiv:1208.1553]

[67] X. Zhang and B. D. Serot, Phys.Rev. **C86**:035502 (2012). [arXiv:1206.6324]

[68] [MiniBooNE+ collaboration], R. Dharmapalan *et al.* (2013). [arXiv:1310.0076]

[69] X. Zhang and B. D. Serot, Phys.Lett. **B719**:409–414 (2013). [arXiv:1210.3610]

[70] *Neutrino-Nucleus Interactions for Current and Next Generation Neutrino Oscillation Experiments*, `http://www.int.washington.edu/PROGRAMS/13-54w/` (2013).

[71] S. Gninenko, Phys.Rev.Lett. **103**:241802 (2009). [arXiv:0902.3802]

[72] S. N. Gninenko, Phys.Rev. **D83**:015015 (2011). [arXiv:1009.5536]

[73] [NOMAD collaboration], C. Kullenberg *et al.*, Phys.Lett. **B706**:268–275 (2012). [arXiv:1111.3713]

[74] J. Conrad, C. Ignarra, G. Karagiorgi, M. Shaevitz, and J. Spitz, Adv.High Energy Phys. **2013**:163897.

[75] G. Mention, M. Fechner, T. Lasserre, T. Mueller, D. Lhuillier, *et al.*, Phys.Rev. **D83**:073006 (2011). [arXiv:1101.2755]

[76] C. Giunti and M. Laveder, Phys.Rev. **C83**:065504 (2011). [arXiv:1006.3244]

[77] G. Karagiorgi (2013). [arXiv:1304.2083]

[78] [LBNE collaboration], C. Adams *et al.* (2013). [arXiv:1307.7335]

[79] [MicroBooNE collaboration], T. Katori, JINST **8**:C10011 (2013). [arXiv:1307.5256]

[80] B. Baptista, L. Bugel, C. Chiu, J. Conrad, C. Ignarra, *et al.* (2012). [arXiv:1210.3793]

[81] C. Chiu, C. Ignarra, L. Bugel, H. Chen, J. Conrad, *et al.*, JINST **7**:P07007 (2012). [arXiv:1204.5762]

[82] B. Jones, J. VanGemert, J. Conrad, and A. Pla-Dalmau, JINST **8**:P01013 (2013). [arXiv:1211.7150]

[83] T. Briese, L. Bugel, J. Conrad, M. Fournier, C. Ignarra, *et al.*, JINST **8**:T07005 (2013). [arXiv:1304.0821]

[84] A. Curioni, B. Fleming, W. Jaskierny, C. Kendziora, J. Krider, *et al.*, Nucl.Instrum.Meth. **A605**:306–311 (2009). [arXiv:0903.2066]

[85] R. Andrews, W. Jaskierny, H. Jostlein, C. Kendziora, S. Pordes, *et al.*, Nucl.Instrum.Meth. **A608**:251–258 (2009).

[86] B. Baptista, L. Bugel, C. Chiu, J. Conrad, C. Ignarra, *et al.* (2012). [arXiv:1210.3793]

[87] V. A. Kostelecky and S. Samuel, Phys.Rev. **D39**:683 (1989).

[88] V. A. Kostelecky and M. Mewes, Phys.Rev. **D69**:016005 (2004). [arXiv:hep-ph/0309025]

[89] J. S. Diaz, V. A. Kostelecky, and M. Mewes, Phys.Rev. **D80**:076007 (2009). [arXiv:0908.1401]

[90] V. A. Kostelecky and M. Mewes, Phys.Rev. **D70**:031902 (2004). [arXiv:hep-ph/0308300]

[91] J. S. Diaz and V. A. Kostelecky, Phys.Lett. **B700**:25–28 (2011). [arXiv:1012.5985]

[92] J. S. Diaz and A. Kostelecky, Phys.Rev. **D85**:016013 (2012). [arXiv:1108.1799]

[93] T. Katori, V. A. Kostelecky, and R. Tayloe, Phys.Rev. **D74**:105009 (2006). [arXiv:hep-ph/0606154]

[94] [LSND collaboration], L. Auerbach *et al.*, Phys.Rev. **D72**:076004 (2005). [arXiv:hep-ex/0506067]

[95] V. A. Kostelecky and N. Russell, Rev.Mod.Phys. **83**:11–31 (2011). [arXiv:0801.0287]

[96] D. Colladay and V. A. Kostelecky, Phys.Rev. **D58**:116002 (1998). [arXiv:hep-ph/9809521]

[97] D. Colladay and V. A. Kostelecky, Phys.Rev. **D55**:6760–6774 (1997). [arXiv:hep-ph/9703464]

[98] V. A. Kostelecky, Phys.Rev. **D69**:105009 (2004). [arXiv:hep-th/0312310]

[99] V. A. Kostelecky and M. Mewes, Phys.Rev. **D70**:076002 (2004). [arXiv:hep-ph/0406255]

[100] [MiniBooNE collaboration], A. Aguilar-Arevalo *et al.*, Phys.Lett. **B718**:1303–1308 (2013). [arXiv:1109.3480]

[101] [MINOS collaboration], P. Adamson *et al.*, Phys.Rev.Lett. **101**:151601 (2008). [arXiv:0806.4945]

[102] [MINOS collaboration], P. Adamson *et al.*, Phys.Rev. **D85**:031101 (2012). [arXiv:1201.2631]

[103] [MINOS collaboration], P. Adamson *et al.*, Phys.Rev.Lett. **105**:151601 (2010). [arXiv:1007.2791]

[104] B. Rebel and S. Mufson, Astropart.Phys. **48**:78–81 (2013). [arXiv:1301.4684]

[105] [IceCube collaboration], R. Abbasi *et al.*, Phys.Rev. **D82**:112003 (2010). [arXiv:1010.4096]

[106] [Double Chooz collaboration], Y. Abe *et al.*, Phys.Rev. **D86**:112009 (2012). [arXiv:1209.5810]

[107] J. Daz, T. Katori, J. Spitz, and J. Conrad, Phys.Lett. **B727**:412–416 (2013). [arXiv:1307.5789]

[108] [OPERA collaboration], T. Adam *et al.*, JHEP **1210**:093 (2012). [arXiv:1109.4897]

[109] A. Kostelecky and M. Mewes, Phys.Rev. **D85**:096005 (2012). [arXiv:1112.6395]

[110] B. Batell, M. Pospelov, and A. Ritz, Phys.Rev. **D80**:095024 (2009). [arXiv:0906.5614]

[111] P. deNiverville, M. Pospelov, and A. Ritz, Phys.Rev. **D84**:075020 (2011). [arXiv:1107.4580]

[112] P. deNiverville, D. McKeen, and A. Ritz, Phys.Rev. **D86**:035022 (2012). [arXiv:1205.3499]

[113] R. Dharmapalan *et al.*, *A Proposal to Search for Dark Matter with MiniBooNE* (2014).

[114] [DAMA Collaboration, LIBRA collaboration], R. Bernabei *et al.*, Eur.Phys.J. **C67**:39–49 (2010). [arXiv:1002.1028]

[115] [CoGeNT collaboration], C. Aalseth *et al.*, Phys.Rev.Lett. **106**:131301 (2011). [arXiv:1002.4703]

[116] G. Angloher, M. Bauer, I. Bavykina, A. Bento, C. Bucci, *et al.*, Eur.Phys.J. **C72**:1971 (2012). [arXiv:1109.0702]

[117] [CDMS collaboration], R. Agnese *et al.*, Phys.Rev.Lett. **111**:251301 (2013). [arXiv:1304.4279]

[118] [SuperCDMS collaboration], R. Agnese *et al.*, Phys.Rev.Lett. **112**:041302 (2014). [arXiv:1309.3259]

[119] [Muon G-2 collaboration], G. Bennett *et al.*, Phys.Rev. **D73**:072003 (2006). [arXiv:hep-ex/0602035]

[120] M. Pospelov, Phys.Rev. **D80**:095002 (2009). [arXiv:0811.1030]

[121] A. Adelmann *et al.* (2012). [arXiv:arXiv:1210.4454 [physics.acc-ph]]

[122] [nuSTORM collaboration], D. Adey *et al.* (2013). [arXiv:1308.6822]

[123] Y.-F. Li, J. Cao, Y. Wang, and L. Zhan, Phys.Rev. **D88**:013008 (2013). [arXiv:1303.6733]